Machine Learning Techniques for Regional Scale Estimation of High-Resolution Cloud-Free Daily Sea Surface Temperatures from MODIS Data

Swathy Sunder[1], RAAJ Ramsankaran[1, 2] and Balaji Ramakrishnan[1]

[1] *Department of Civil Engineering, Indian Institute of Technology Bombay, Powai, Mumbai 400 076, India.*

[2] *Interdisciplinary Program in Climate Studies, Indian Institute of Technology Bombay, Powai, Mumbai 400 076, India.*

Corresponding Author:

RAAJ Ramsankaran

Hydro-Remote Sensing Application Group

Department of Civil Engineering, IIT Bombay, *Powai, Mumbai 400 076, India.*

Email : ramsankaran@civil.iitb.ac.in

Abstract

High-resolution sea surface temperature (SST) estimates are dependent on satellite-based infrared radiometers, which are proven to be highly accurate in the past decades. However, the presence of clouds is a big stumbling block when physical approaches are used to derive SST. This problem is more prominent across tropical regions such as Arabian Sea(AS) and Bay of Bengal(BoB), restricting the availability of high-resolution SST data for ocean applications. The previous studies for developing daily high-resolution cloud-free SST products mainly focus on fusion of multiple satellites and in-situ data products that are computationally expensive and often time consuming. At the same time, it was observed that the capabilities of data-driven approaches are not yet fully explored in the estimation of cloud-free high-resolution SST data. Hence, in this study an attempt has been made for the first time to estimate daily cloud free SST from a single sensor (MODIS Aqua) dataset using advanced machine learning techniques. Here, three distinct machine learning techniques such as Artificial Neural Networks (ANN), Support Vector Regression (SVR) and Random Forest (RF)-based algorithms were developed and evaluated over two different study areas within the AS and BoB using 10 years of MODIS data and in-situ reference data. Among the developed algorithms, the SVR-based algorithm performs consistently better. In AS region, while testing, the SVR-based SST estimates was able to achieve an adjusted coefficient of determination (R^2_{adj}) of 0.82 and root mean square error (RMSE) of 0.71°C with respect to the in situ data. Similarly, in BoB too, the SVR algorithm outperforms the other algorithms with R^2_{adj} of 0.78 with RMSE of 0.88ºC. Further, a spatio-temporal and visual analysis of the results as well as an inter-comparision with NOAA AVHRR daily optimally interpolated global SST (a standard SST product available in practice) the suggest that the proposed SVR-based algorithm has huge potential to produce

operational high-resolution cloud-free SST estimates, even if there is cloud cover in the image.

Keywords: cloud-free SST, SVR, ANN, RF, MODIS

1. Introduction

Sea Surface Temperature (SST) is considered as one of the fundamental geophysical variables, used to define the physical environment and the variability of aquatic ecosystems. Moreover, the spatial and temporal patterns of SST are having a significant impact on the health and sustainable management of fisheries environments (Santos, 2000; Delgado et al., 2014; Williams et al., 2010). On the other hand, SST is an essential variable in the modelling of oceanography, marine weather, etc. and it is a crucial variable to assess the effects of global warming on the upper layer of the ocean, which is an indicator of the health of coastal ecosystems (Barnes and Hu, 2013). Hence, mapping and monitoring the SST fields are one of the important tasks of oceanographers.

Nowadays, satellite remote sensing-based approaches are the norm to map and to monitor SST globally, which offers high spatial and temporal resolution. The most accurate estimates of SST from space are the infrared radiometer-based estimates in cloud-free conditions (Barton, 2001). The monitoring of SST using satellite infrared radiometers started since 1981 when National Oceanic and Atmospheric Administration (NOAA) launched Advanced Very High-Resolution Radiometer (AVHRR) sensor onboard on NOAA 7 satellite (Delgado et al., 2014). Following this, during May 2002, National Aeronautics and Space Administration (NASA) launched Moderate Resolution Imaging Spectroradiometer (MODIS) on Aqua platform. NASA distributes MODIS Aqua level 2 SST fields which has daily coverage, 1 km spatial resolution and high correlation with the in situ data (Wang and Deng, 2017; Chavula

et al., 2009) and lowest bias (0.1–0.3 K) globally compared to other platforms including MODIS Terra (Tomazic et al., 2011; Wang and Deng, 2017).

NASA Ocean Biology Processing Group (OBPG) uses a non-linear sea surface temperature(NLSST) algorithm to estimate SST values from far infrared bands (Brown and Minnett, 1999). This approach holds good for global oceans but often suffers from cloud cover problems. The tropical regions have more clouds compared to the higher latitudes (NASA, 2019), which result in huge data loss. This will restrict the data availability for coastal applications, especially during the monsoon time (LaCasse et al., 2008). Though the microwave (MW) radiometers can provide SST estimates in the cloudy conditions, the error is larger due to several issues such as large footprints, the need for atmospheric absorption correction and the strong dependency of surface emissivity with the surface roughness and wind speed (Barton, 2001).

Several approaches are available to estimate cloud-free SST fields using different combinations of IR and microwave sensors viz. IR–IR combinations, MW-MW combinations and IR–MW combinations. Operational Sea Surface Temperature and Sea Ice Analysis reanalysis (OSTIA_RAN) product by Stark et al. (2008) and AVHRR Optimally Interpolated (OI) near real-time product by Reynolds et al. (2007) are some of the attempts made to combine IR–IR sensors data. Remote Sensing System's MW OI near real-time product is an example of MW–MW sensors combination SST products (RSS, 2019). Examples of different IR–MW sensor combinations are ODYSSEA (Autret and Piolle, 2011), Geostationary Operational Environmental Satellite—Polar Operational Environmental Satellites (GOESPOES) SST product (Maturi et al., 2008), Multi-scale Ultra-high-Resolution Sea Surface Temperature (MUR SST) (Chin et al., 2017), etc. Due to the difference in satellites overpass time in a region, the multi-sensor approaches will consume more time to capture the images itself and it would be unfavourable for near real-time applications.

Most of the operational products for estimating cloud-free SST are typically based on optimum interpolation (OI) approach, for example, cloud-free OSTIA (Donlon et al. 2012), Canadian Meteorological Centre (CMC) 0.2°SST (Brasnett, 2008), ODYSSEA(Autret and Piolle,2011) and AVHRR_AMSR OI (Reynolds et al., 2007). Also, these model-driven approaches require prior information about the decorrelation scales and covariance functions. Currently, majority of these global daily SST products have typical grid resolution ranging between 0.05° ×0.05° and 0.25° ×0.25°, or approximately between 5 and 25 km. In such cases, actual resolution of the geophysical products can be significantly coarser than the grid resolutions due to spatial and temporal averaging applied for interpolation (Reynolds and Chelton, 2010). To the best of the authors' knowlededge, till date only three attempts (Chao et al. 2009, Buongiorno Nardelli et al. 2013 and Chin et al. 2017) have been made to provide cloud-free SST products at 0.01 × 0.01 grid resolutions. These three studies, which are based on the multi scale approaches are complex and require a lot of assumptions (Miles and He, 2010; Fablet et al., 2018; Zhao and He, 2012). At the same time several past studies related to remote sensing of geophysical varaiables (Picart et al., 2018; Wang and Deng, 2017; Lary et al., 2016) show that machine learning (ML) techniques could provide a convenient way to work around complex problems, especially for remote sensing data. Hence, ML is considered to be a practical approach for both classification and regression of non-linear systems and often called as "Universal approximators" as they learn the underlying behaviour of a system from a set of training samples (Alavi et al., 2016). The most significant advantage of these techniques that is they do not need any prior information regarding the nature of the relationship between the data (Lary et al., 2016)

Machine Learning comprises a number of techniques such as Artificial Neural Networks (ANN), Support vector machines/support vector regression (SVM/SVR), decision trees, self-organising map, ensemble methods such as random forests, neuro-fuzzy, genetic algorithm

and multivariate adaptive regression splines. Among these techniques, ANN and SVM/SVR are the most commonly used in geoscience problems (Lary et al., 2016; Lary, 2010). Some of the recent studies show that random forest-based algorithms perform better than other ML techniques while addressing various problems in the field of remote sensing (Liu et al., 2015; Belgiu and Dra, 2016; Picart et al., 2018; Cracknell and Reading, 2014; Liu et al., 2014). Many researchers pointed out that ANN, SVM/SVR and random forest-based algorithms are characterised by self-adaptability, swift learning pace and limited requirement of training size, which makes them reliable in intelligent processing of remote sensing datasets (Lary et al., 2016; Mountrakis et al., 2011; Lary, 2010). Moreover, the machine learning-based approaches do not involve an explicit characterisation of surface and/or atmospheric parameters but require only in situ datasets for training purpose (Moser et al., 2009).

Till date, the efforts to develop daily high-resolution cloud-free SST products mainly focused on fusion of multiple satellite and in situ data products, which involves complex computations and they are computationally expensive as well as time-consuming, thus limiting their applications for any real-time applications. However, for near real-time applications, singe sensor-based cloud-free SST products will be more useful as the data will be available soon after the satellite overpass. At the same time, machine learning algorithms are useful in the estimation of various geophysical variables even during sparse data conditions, but its capabilities were still not assessed for estimation of cloud-free SST. For example, Wang and Deng, 2017 developed an ANN based approach to estimate SST, however, they had not attempted to address the data gap due to clouds.

Therefore, to address the mentioned research gaps, this study focuses on utilising single sensor data for developing new algorithm(s) for estimating high-resolution cloud-free regional SST fields on a daily basis using machine learning techniques. In order to select the best machine learning technique, here we have explored and compared three different widely

used techniques viz. artificial neural networks, support vector regression and random forest for its predictive accuracy to estimate surface temperature irrespective of cloud cover.

2. Study Area and Datasets

Two different study areas were selected for this research work. Study area –I is the south eastern part of the Arabian Sea (AS) along the Indian Coastline (Figure 1). This area is within the tropical latitude and longitudinal extent of 5 ° to 23° N and of 60° to 78° E. Study area – II is the northern parts of Bay of Bengal (BoB) which lies between the latitudes 12 ° to 22° N and longitudes of 82° to 95° E (Figure 2). Since both study areas are situated in the similar latitude bands that lie in the tropics; there is a significant amount of cloud cover in the region compared to the higher latitude regions (NASA, 2019). However, both the study areas have striking dissimilarities especially in terms of wind and precipitation charecterestics. For example, the winds over the two basins are different. The main reason is that the presence of highlands of East Africa in the boundary of AS region results in atmospheric "western boundary current" (Anderson, 1976), which makes the winds over AS more than twice as strong as those over the BoB. Unlike AS, precipitation exceeds evaporation in the BoB. BOB receives runoff from major rivers such as Ganga and Brahmaputra into the northern bay while the runoff from rivers into AS is meagre. Therefore, the surface layer in the BoB is much fresher than that in the AS; resulting in a higher salinity in the AS. As a consequence, typical profiles of temperature and salinity in the two basins differ considerably. Due to the massive inflow of freshwater from precipitation and runoff, strong near−surface stratification is observed in BoB (Shenoi et al., 2002).

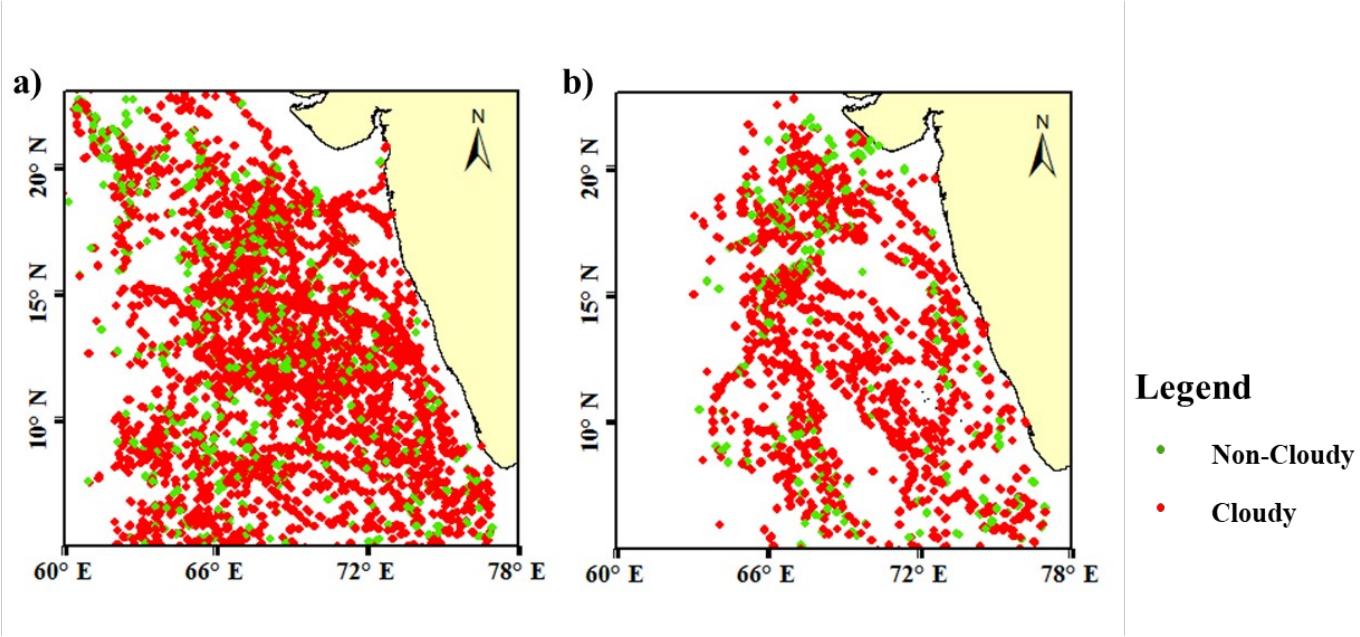

Figure 1: Spatial distribution of in-situ data points in AS. (a) Training data points. (b) Testing points.

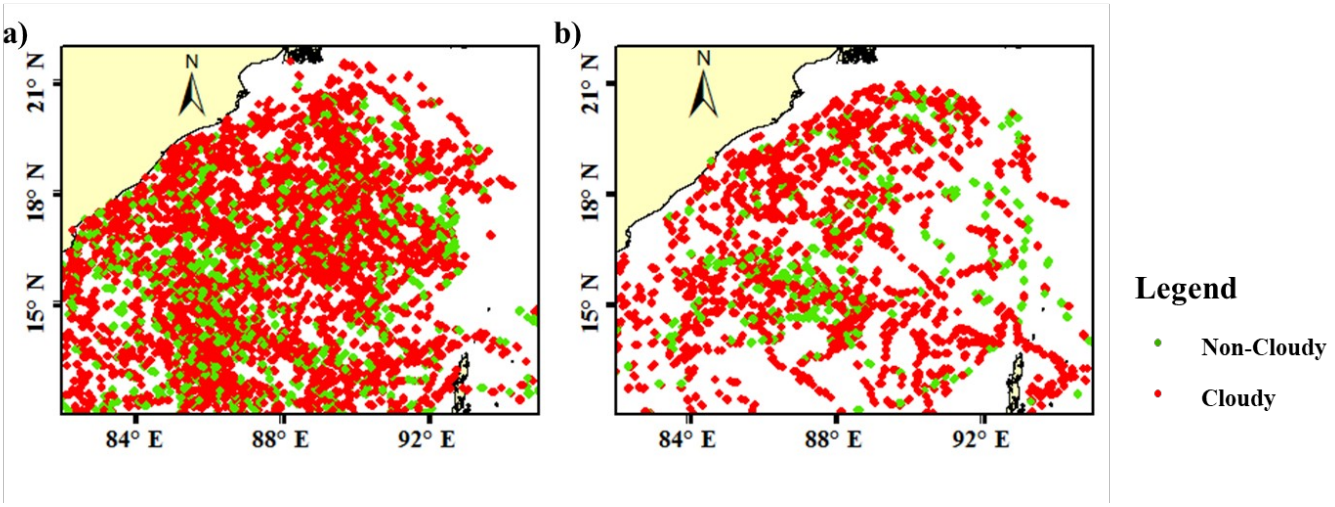

Figure 1: Spatial distribution of in-situ data points in BoB. (a) Training data points. (b) Testing points

Datasets: The study involves use of satellite and in-situ data of nine years from January 2006 to December 2015. Here, the MODIS Aqua satellite data was selected because they are available on daily scale at 1 km grid resolution. Moreover, studies have pointed out that MODIS Aqua shows the least bias compared to other platforms (Tomažić et al., 2011; Wang and Deng, 2017). Accordingly, MODIS Aqua daytime level 0 (L0) data was downloaded

175 from NASA Ocean Color website (NASA,2014) for the study period and processed to
176 achieve level 2 (L2) data for further use in the modelling.

177 The in-situ SST data used in this study were obtained from the Centre ERS d'Archivage et de
178 Traitement (CERSAT)—French ERS Processing and Archiving Facility (CERSAT, 2018).
179 CERSAT collects surface-level in-situ SST data from Coriolis data center and distributes it,
180 in an easier-to-use format, which can be compared with the satellite SST products.
181 Distribution of the data points used in this study for AS and BoB regions are shown in
182 Figures 2 and 3 respectively. Data collected during the years 2006–2013 were used for
183 training and the data collected during 2014-2015 were used for independent testing. We have
184 used only those in- situ datasets which have been collected within ±3hrs of the satellite
185 overpass. Characteristics of the in-situ data used in this study are mentioned in Table.1. It
186 shall be noted that 82% of the training data and 81% of the testing data were under cloud
187 cover for AS. Whereas, for BoB it is 76% and 79% respectively.

188 *Table 1: Satistical Characterestics of in-situ data.*

Statistics	AS Training	AS Testing	BoB Training	BoB Testing
Mean (ºC)	28.79	28.38	28.08	28.11
Standard deviation(ºC)	1.42	1.62	1.44	1.83
Minimum(ºC)	22.6	21.2	22.6	21.4
Maximum (ºC)	34 .2	33.9	33.6	34.6
Percentage of Cloud Cover(%)	82	81	76	79

189

190 At the same time, the NOAA AVHRR_OI-NCEI-L4-GLOB-v2.0 daily SST (Hereafter
191 reffered as NOAA SST in this manuscript) product (Reynolds et al., 2007; NCEI, 2016) was
192 also used during the independent testing period in order to compare with the ML-based SST
193 outputs derived in this study. This daily scale product, which is based on optimal
194 interpolation of AVHRR, NCEP ice, and in-situ datasets, gives cloud-free bulk SST values at
195 25 km resolution across the globe. This NOAA SST is a valuable product to be

intercompared with the estimates obtained herei because the present study also aims to compute daily scale cloud-free bulk SST at high spatial resolution.

3. Methods

The overall framework adopted for this study is described as a flowchart in Figure 3. MODIS (Aqua) L0 datasets are selected for this study since they can be downloadable immediately after the satellite overpass, thereby useful in near real-time applications. As an initial step, MODIS L0 data were processed to obtain L2 Brightness Temperature (BT) values using SeaWiFS Data Analysis System (SeaDAS) (Baith et al., 2001) as follows. Firstly, the MODIS Level 0 -Product Data Set (MODIS L0 – PDS) were converted to Level 1A file using the python script modis_L1A.py, available in SeaDAS. Further, the corresponding geo-location file was derived from Level 1A file using the modis_GEO.py. Following that, Level 1A and Geo files were used as inputs for the modis_L1B.py to generate Level 1B file that contain calibrated and geolocated at-aperture radiance. Finally, the brightness temperature at 11 and 12 micrometres are generated using l2gen SeaDAS script.

In this study, six different variables have been used to develop algorithm(s) for estimating SST through three different ML techniques. The selection of inputs was done by referring the available scientific literature. Among the input variables, the brightness temperatures at 11- and 12-micrometre channels are considered to be the most important and necessary quantities to estimate SST from space(Brown and Minnett, 1999; Barton, 2001, Wang and Deng, 2017) and hence, the same are adopted in this study. Likewise, studies conducted by Alavi et al., 2016 and Picart et al., 2018 have proven that latitude and longitude have significance in deriving SST using data-driven approaches and hence, they are incorporated in this study. At the same time, the Julian day is also reported as one of the important variables to estimate SST to account for the seasonal characteristics (Sirjacobs et al., 2011) and hence, it is also

considered here. Lastly, variable cloud factor (CF) is also introduced in the algorithm to indicate the presence of clouds. If CF = 1, there is cloud and if CF = 0, there is no cloud, and this value can be obtained from MODIS cloud mask. The model outputs were analysed for different set of inputs. It was found that the best results could be achieved when all the inputs used in the model. It shall be noted that all these inputs can be extracted as soon as the satellite image is available, which makes them desirable for operational purposes. All inputs were normalised to the range of 0 and 1 before training and testing in order to make all columns in the dataset using a common scale as given in LaCasse et al. (2008).

Here, the training and testing of the samples were done in two different scenarios. In Scenario-1, cloudy and non-cloudy pixels were trained together. In this case, the variable CF was used to distinguish between cloudy and non-cloudy pixels. In Scenario-2, the cloudy pixels and non-cloudy pixels were trained and tested separately. Hence, for Scenario-2, CF variable was not used. All three ML techniques were trained using the datasets collected during the years 2006–2013 and tested using the datasets of 2014-2015. Ten-fold cross-validation method was used for training the samples as it involves the training and validation of the entire dataset, which will make the model robust with improved generalisation capabilities.

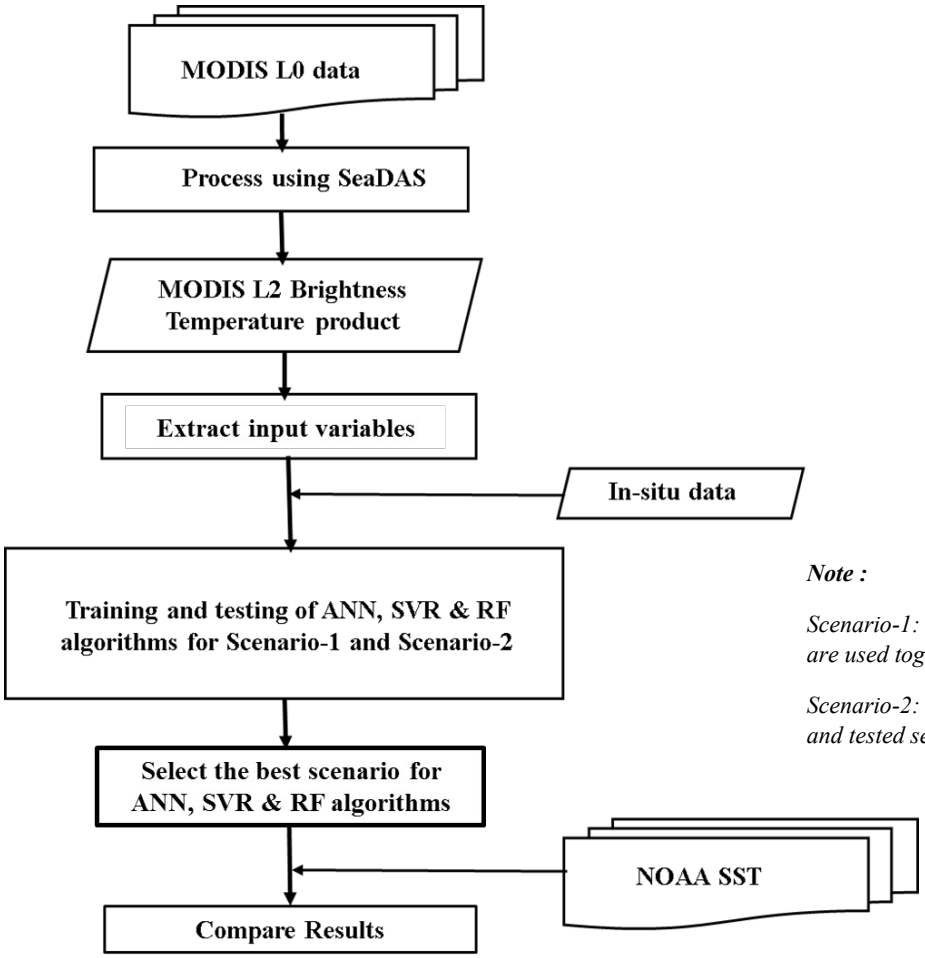

Figure 3: Overall framework of the present study.

3.1 Description of the selected ML Techniques

In this research, Weka software by Witten et al., (2016) has been exploited to develop ML based SST algorithms. Description of the selected ML technique(s) is discussed as follows.

a. Artificial Neural Networks

The Artificial Neural Networks (ANNs) used in this study are the conventional feed-forward neural networks, also known as multi-layer perception. Generally, ANN consists of three or more interconnected nodes or layers: an input layer, output layer, and one or more hidden layers. The readers are referred to Havkin (1990) for more explanations regarding the differences configurations of neural networks. In ANN, an input vector x^N is passed through a

series of non-linear hidden neuron activation functions G(.) to an output layer $\widehat{f(x)}$ via a series of optimised weight matrices wj.

The output of the network is given by Eqn. (1)

$$\widehat{f(x)} = f\left\{\sum_{j=1}^{h} w_j G(s_i) + b_k\right\} \quad (1)$$

where f is the activation function of the output neuron k, b_k is the bias of the output neuron and s_i is the weighted sum of the input data to the hidden neuron activation functions for each layer j. Let the training dataset be $D=\{x^n, t^n\}_{n=1}^{N}$. The network is trained using input dataset by adjusting the parameters w, to minimise the error function E_D. The error function is given by Eqn. (2).

$$E_D = \frac{1}{N}\sum_{n=1}^{N}\{y_n(x^n; w) - t_n\}^2 \quad (2)$$

For each input/target pair {x,t}, the output $\widehat{f(x;w)}$ is calculated for the entire series to calculate the error between the network output and target. The minimisation of error is carried out by repeated evaluation of the gradient of E_D using the variants of batches k propagation algorithm. After various trials, it was found that 25 hidden neurons in two layers each containing 10 and 15 neurons are chosen as optimal values.

b. Support Vector Regression

Support vector machine (SVM) is a supervised non-parametric statistical learning technique (Mountrakis, Im, and Ogole, 2011b) initially formulated by Vapnik (1979). The main objective of the SVM algorithm is to find a hyperplane that separates the dataset into a number of classes in such a way that it is consistent with the training examples. Generally, the regression based on support vector machines (SVRs) can be explained as follows:

SVM estimates $\hat{f}$ by minimising an upper bound on the probability that the estimation error may be above a given threshold (Moser et al., 2009). For a set of training samples

$\{(x_1, y_1),(x_2, y_2),(x_3, y_3),\ldots(x_h, y_h),\ldots(x_N, y_N)\}$ of sample size N (where $x_h$is the h[th] feature vector corresponding to the reference measurement y_h; h=1,2,3,….N), the resulting approximation can be expressed as a linear combination of suitable kernel functions centred on a subset of training samples as given by Eqn.(3) (Moser et al., 2009; Vapnik, 1998).

$$\widehat{f(x)} = \sum_{h \epsilon S} \beta_h^{¿} K(x_h, x \vee \gamma) + b^{¿} \quad (3)$$

where $\beta_1^{¿}, \beta_2^{¿} \ldots \beta_N^{¿}$ are the weight coefficients of the linear combination, K(·, .¿γ) is a kernel function, in general, by a vector γ of r real valued parameters ($\gamma \epsilon R^r$),$b^{¿}$ is a bias term, and $S = \{h : \beta_h^{¿} \neq 0\}$. If $h \in S$, i.e., $\beta_h^{¿} \neq 0$, the training sample x_h is named 'support vector' (Moser et al., 2009; Vapnik, 1998).

Selection of kernel functions play a vital role in the performance of the support vector machines. In this study, Pearson VII function kernel generally known as PUK is used as it can be served as a universal kernel. Studies (Zhang and Ge, 2013; B. Ustun, Melssen, and Buydens, 2006) have proven that PUK kernel is robust with an equal or even stronger mapping power compared to the other standard kernel functions (linear, Polynomial and RBF kernel functions) used in SVMs.

c. Random Forest

The working principle of the random forest is as follows: The technique applies P random samplings with replacement as given in Eqn. (4)

$$\widehat{f(x)} = \frac{1}{P} \sum_{i=1}^{P} t_i(x_1, \ldots x_N) \quad (4)$$

where t_i is the different regression tress (Breiman, 2001; Picart et al., 2018). Each tree is based on a simple decision criteria on X covariates such as: if X< threshold, then value 1 else value 2. The threshold value is calculated with respect to the training samples by maximising

the difference between value 1 and value 2. The dataset will be split further recursively at each node of the tree.

For the present study, a maximum of 2500 nodes and a forest consisting of 300 trees have been considered. The maximum number of nodes was selected on trial and error basis by increasing the number of nodes from 100 to 4000 trees.

3.2 Evaluation of the results

The developed ML based algorithms were evaluated for two different scenarios. In scenario-1, the algorithms were trained using both cloudy and non-cloudy pixels together. In scenario-2, the algorithms were trained separately for cloudy and non-cloudy pixels. Accordingly, the performances of each developed algorithm were analysed for both scenarios based on adjusted R^2 (R^2_{adj}), Root mean square error (RMSE) and mean absolute error (MAE) values. Generally, R^2 is used as a measure of the proportion of variance of the predicted results. However, in this study R^2_{adj} has been used to assess the algorithm performance in order to adjust the model results with the number of predictors. RMSE and MAE were calculated for assessing total error values in the algorithms. By squaring the error, before calculating the mean and later taking the square root gives more weight to large but infrequent errors than the mean in RMSE. Therefore, comparison of RMSE and MAE can be used to determine whether the forecast contains large but infrequent errors. Larger the difference between RMSE and MAE, more inconsistent the error size is.

For the identified best scenario of each algorithm, spatial and temporal distribution of errors of individual points were calculated as follows. Difference between the in-situ SST (SST_{ref} ¿ and the predicted SST ($\widehat{SST}$ ¿ values was computed for each data point (Eqn.5)

$$\Delta SST = \left(SST_{ref} - \widehat{SST} \right) \quad (5)$$

316 ΔSST values were then analysed spatially for both training and testing phase. Further, ΔSST
317 values for each Julian day are averaged and the temporal distribution of the error values is
318 studied. Finally, the best performing ML SST estimates were inter-compared with a standard
319 cloud-free daily SST product (NOAA SST) against the reference in-situ data.

320 ## 4. Results and Discussions

321 The obtained results are discussed in four sub-sections. First, in section 4.1, the results of the
322 algorithm(s) developed for both scenarios are discussed. In sections 4.2 and 4.3, the results
323 from the best scenario are analysed both spatially and temporally to study the error
324 distribution. In Section 4.4, an inter-comparison of the best performing ML SST estimate and
325 NOAA SST with respect to in-situ data is presented. Finally, in Section 4.5 some illustrative
326 examples of the SST images for pre-monsoon, monsoon and post-monsoon seasons are
327 presented for visual analysis of the algorithm(s) outputs.

328 ### 4.1 Performance of the developed ML algorithms during training and testing phases

329 Overall performance of the developed ML-based algorithms during training and testing for
330 both scenarios are shown for both AS and BoB regions in Figures 4a–d and 5 a-d
331 respectively. It is evident that all the developed algorithms perform relatively well
332 considering the significant amount of cloud contamination in the study regions. However,
333 SVR algorithm performs consistently better than the other two tested algorithms in both
334 Scenario-1 and Scenario-2.

335 #### 4.1.1 Study area I : AS

336 In Scenario-1, during training (Figure 4a), R^2_{adj} for RF is higher than that of SVR and ANN.
337 The error values (RMSE and MAE) also indicate that RF has the least error followed by SVR
338 and ANN. However, for the same Scenario-1 while testing, SVR shows the highest R^2_{adj} of

0.86 followed by ANN and RF (Figure 4b). Likewise, the magnitude of error values is also lowest for SVR algorithm followed by ANN and RF algorithms. These indicate that RF algorithm performs inconsistently compared to SVR and ANN. From Scenario-2 results (Figure 4c and d), it can be observed that all the three algorithm s perform almost similar to Scenario-1 during both training and testing phases.

The maximum difference of 0.2°C between RMSE and MAE values for all three algorithms in both scenarios indicates that the occurrence of very large but infrequent errors is not significant.

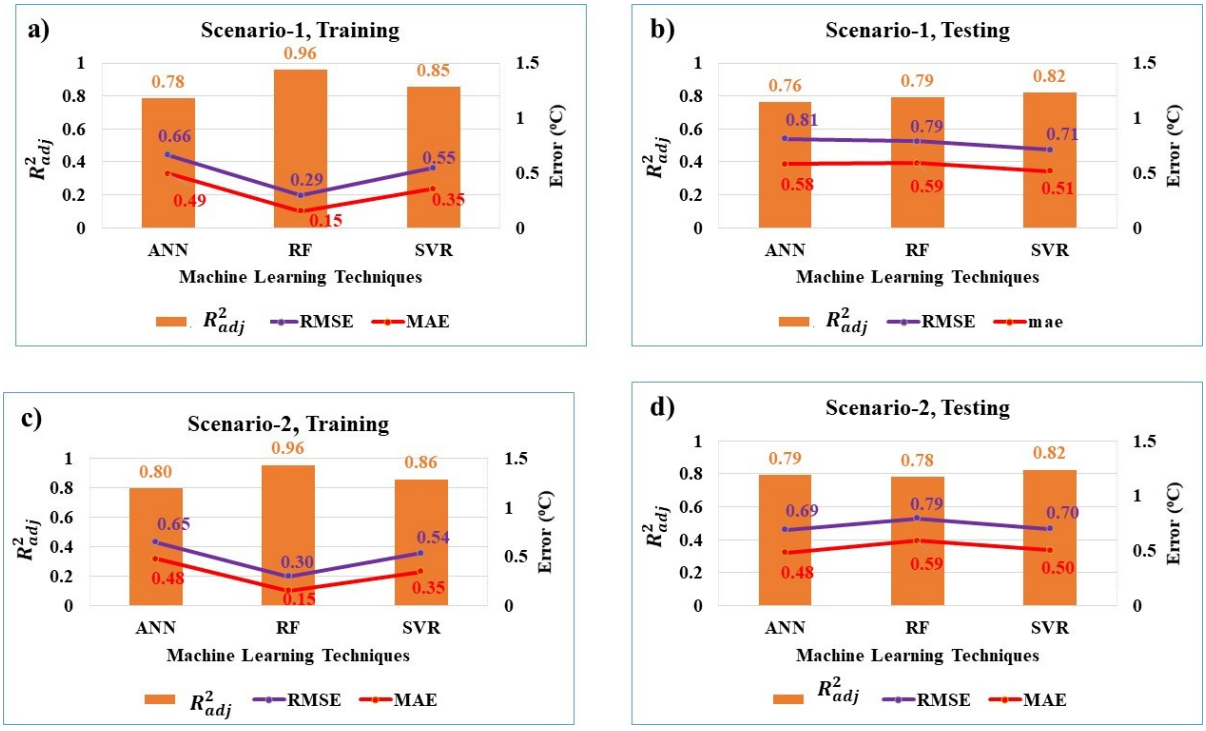

Figure 4: Performance of the developed ML based algorithm(s) in AS for Scenario-1: training (a) and testing (b) and Scenario-2: training (c) and testing (d).

4.1.2 Study area II: BoB

Performance of the algorithms in BoB is similar to that of AS. In Scenario-1, during training phase(Figure 5a), R^2_{adj} for RF is higher than that of SVR and ANN. Accordingly, RF showed the least error values followed by SVR and ANN. Similar to AS, for Scenario-1 while testing,

SVR and RF shows the highest R^2_{adj} followed by ANN (Figure 5b) and the error values are lowest for SVR algorithm followed by RF and ANN algorithms. In BoB too, all the three algorithms perform almost similar in both Scenario-1 and Scenario-2 during training and testing phases. However, there is a slight decrease in the overall performance of the developed ML algorithms in BoB compared to AS. As mentioned in Section 2, BoB is more complex in nature than AS. The presence of strong near-surface stratification due to large inflow of precipitation and runoff (Shenoi et al., 2002) could be the reson for relatively poor performance of the tested algorithms in BoB.

By analysing the results of the two different study regions, it is observed that there is no considerable difference between the results of both scenarios during training and testing phases. Hence, it is better to choose a single model as given in Scenario-1 to reduce the model complexity and runtime. Therefore, only Scenario-1 results are considered for further testing and analysis.

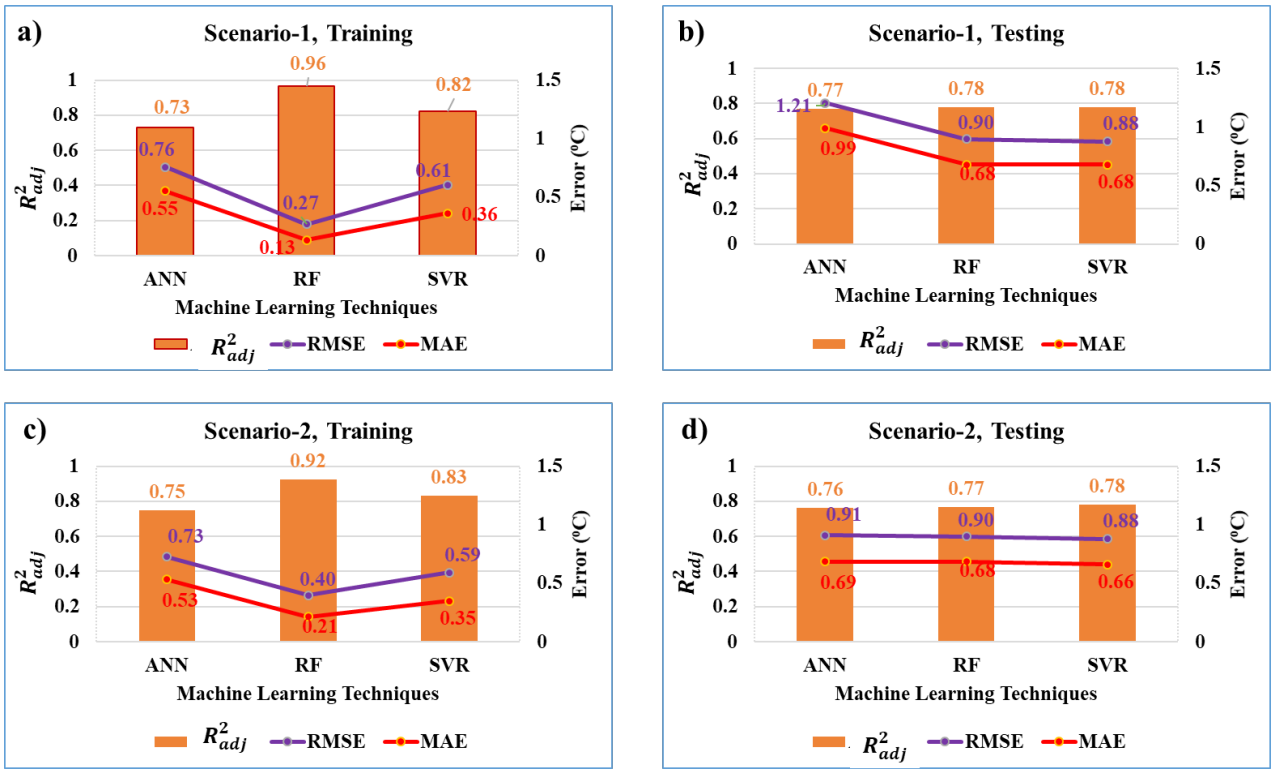

368 *Figure 5:: Performance of the developed ML-based algorithm(s) in BoB for Scenario-1:*
369 *training (a) and testing (b) and Scenario-2: training (c) and testing (d).*

370

371 **4.2 Spatial analysis of the results**

372 Outputs of the ML based models developed for Scenario -1 were analysed spatially to obtain
373 the distribution of errors in individual data points during training and testing periods,
374 respectively.

375 **4.2.1 Study area I: AS**

376 The overall spatial distribution of ΔSST values for training and testing as well as the number
377 of points in each range of ΔSST is given in Figures 6a-h. From Figures 6a-d, it can be
378 observed that all three developed algorithms perform relatively well during the training
379 period, but the ANN algorithm gives larger ΔSST values compared to the other two
380 algorithms. During training, 89% of the data points have ΔSST values within $\pm 1^{0}$C for ANN
381 algorithm, whereas for RF and SVR algorithms, it is 98% and 93% respectively. Likewise,
382 the distribution of errors obtained in AS while testing the algorithms (Figures 6e-h) shows
383 that the RF algorithm gives larger ΔSST values followed by ANN and SVR algorithms. The
384 percentage of data points having ΔSST values within $\pm 1^{0}$C is 84%, 81% and 88% for ANN,
385 RF and SVR algorithms respectively. This results indicate that SVR algorithm has good
386 generalisation capabilities as it could predict most of the variations with least error values
387 during both training and testing periods.

388 **4.2.2 Study area II : BoB**

389 Figures 7a-h show the overall spatial distribution of the ΔSST values for training and testing,
390 inlcuding the number of points in each range of ΔSST. The variations of ΔSST values during
391 training are given in Figures 7a-d. Similar to AS, the occurrence of larger errors is very less

during the training period for all the developed algorithms.While training, RF algorithm has the least error values with 98% of data points has ΔSST values within $\pm 1^{0}C$ followed by SVR (92%) and ANN(85) algorithms. It can be observed that while testing (Figure 7e & h) ANN algorithm shows larger error values. Only 58% of the data points has ΔSST values within $\pm 1^{0}C$ for ANN algorithm, whereas it is 77% and 78% for RF(Figure 7b & f) and SVR(Figure 7c & g) algorithms respectively.

Overall, it is observed that the SVR algorithm is working better for both AS and BoB regions in terms of error values although the performance of the former is slightly lower in BoB. The relatively poor performance of all the tested algorithms in BoB could be due to the similar reasons discussed in Section 4.1. Also, it is noteworthy that though a majority of pixels are cloud-covered during both training and testing (Figure 1&2), all the three developed ML algorithms are capable of producing SST estimates with high accuracy, albeit with minor differences. Thus, it can be said that the ML based algorithms will aid the ongoing efforts of the research groups like The Group for High-Resolution Sea Surface Temperature (GHRSST) for estimating SST at high spatial resolutions from space.

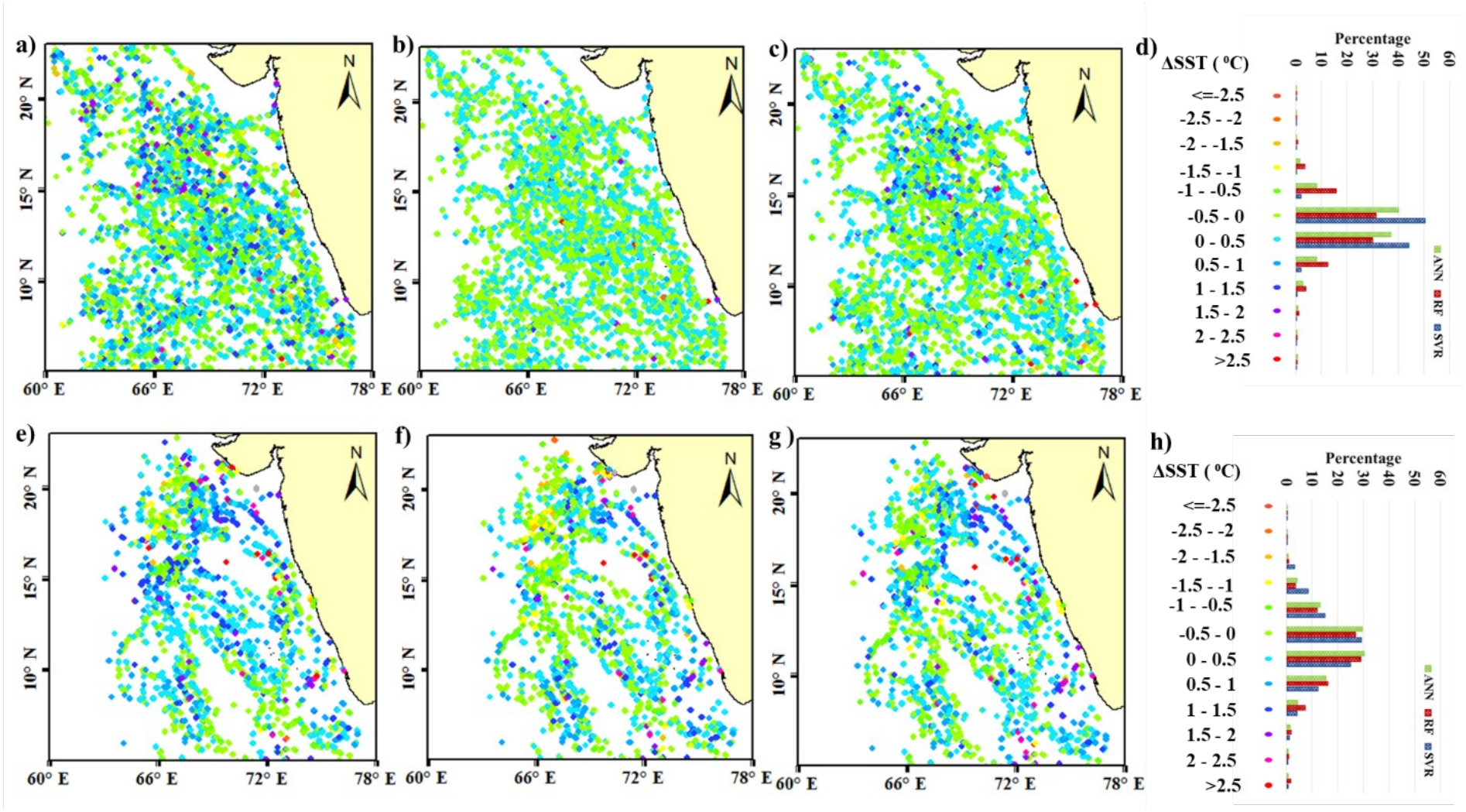

Figure 6: Spatial distribution of $\Delta SST\,(SST_{ref} - \widehat{SST}$ ¿ *values in degree Celsius across the AS during training (a-c) and testing period (e-f) for ANN, RF and SVR respectively. Sub-figures (d) and (h) show number of points (in percentage) in various ranges of* ΔSST *during training and testing periods.*

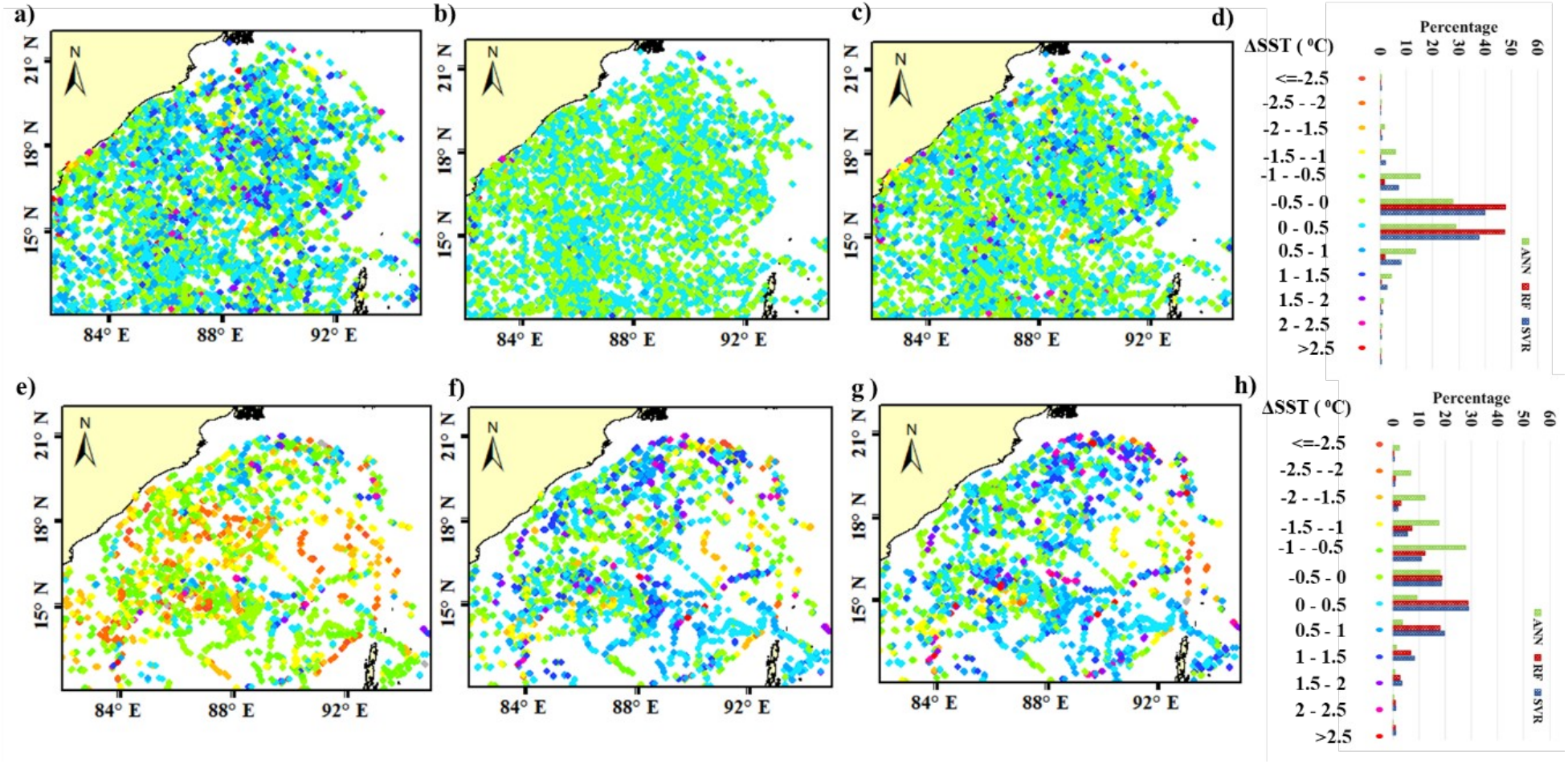

Figure 6: Spatial distribution of $\Delta SST\,(SST_{ref} - \widehat{SST}$ ¿ values in degree Celsius across the BoB during training (a-c) and testing period (e-f) for ANN, RF and SVR respectively. Sub-figures (d) and (h) show number of points (in percentage) in various ranges of ΔSST during training and testing periods.

4.3 Temporal analysis of the results

The results obtained from the ML based models developed for Scenario -1 in both the study regions were temporally analysed to visualise the average error distribution in a year.

4.3.1 Study area I : AS

The number of reference points in each julian day and the average ΔSST values for the corresponding day during training and testing period are given in Figures 8a-d. In training phase, all the developed algorithms show a mixed trend of underestimation and overestimation (Figure 8a–b). The magnitude of error is higher for the ANN algorithm, followed by SVR and RF algorithms. During the monsoon period, that is from Julian day 152 to 273, large error values were expected due to intense cloud cover. However, the ΔSST values for all the three algorithms during monsoon time are quite similar to the other days (Figure 8b).

Likewise, the number of points and average ΔSST values on each Julian day during the testing period are plotted in Figures 8c–d. All the developed algorithms severely underestimate during the first two calendar months compared to other months in the testing period. Studies conducted by Thadathil et al.,1992 and Balachandran et al., 2008 reported about the temperature inversions in AS during winter. This could be the reason behind the severe underestimation of the algorithms during the same time. ANN algorithm shows the largest magnitude ΔSST values during the testing phase compared to the other tested algorithms. Unlike the training phase, the RF algorithm shows larger magnitude of errors while testing (Figure 8d). SVR algorithm shows similar performance during training as well as testing and also it gives the least average ΔSST values in the testing phase. Hence, in terms of the error magnitude, SVR algorithm is more reliable compared to the other two algorithms.

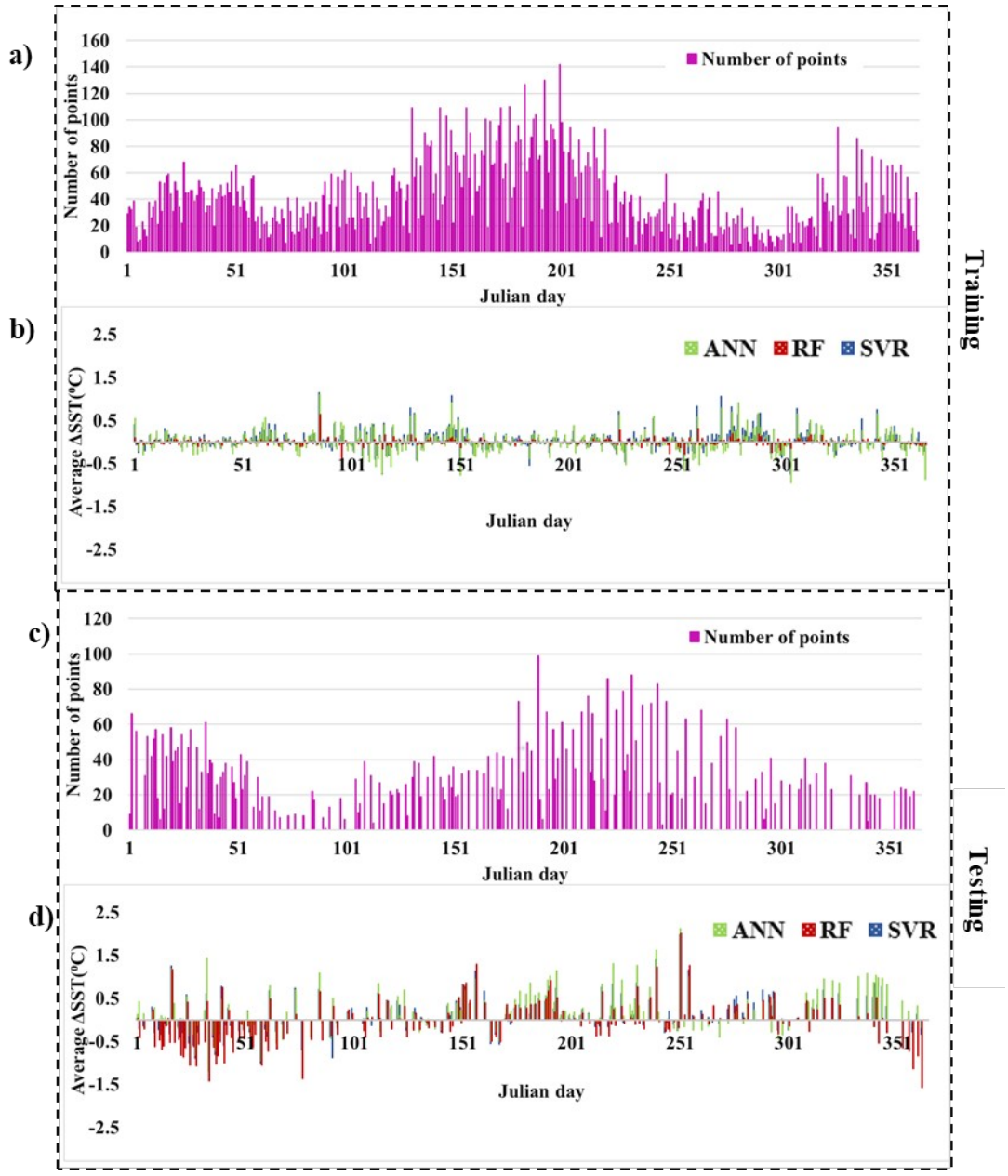

436

437 *Figure 8: Number of reference points available in each Julian day and Average ΔSST* ($SST_{ref} - \widehat{SST}$)
438 *in degree Celsius for the corresponding day during training (a-b) and testing(c-d) periods*
439 *respectively for AS.*

440 **4.3.2 Study area II : BoB**

441 Similar to AS region, the temporal distribution of reference points and average ΔSST values
442 for BoB during training and testing period are given in Figures 9a-d. For the training period
443 (Figures 9 a–b), the magnitude of average *ΔSST* is higher for the ANN algorithm, followed by
444 SVR and RF algorithms throughout the year. From Figure 9c-d, it can be observed that ANN

is showing the larger magnitude of average ΔSST values compared to the other algorithms followed by RF and SVR during the testing period.

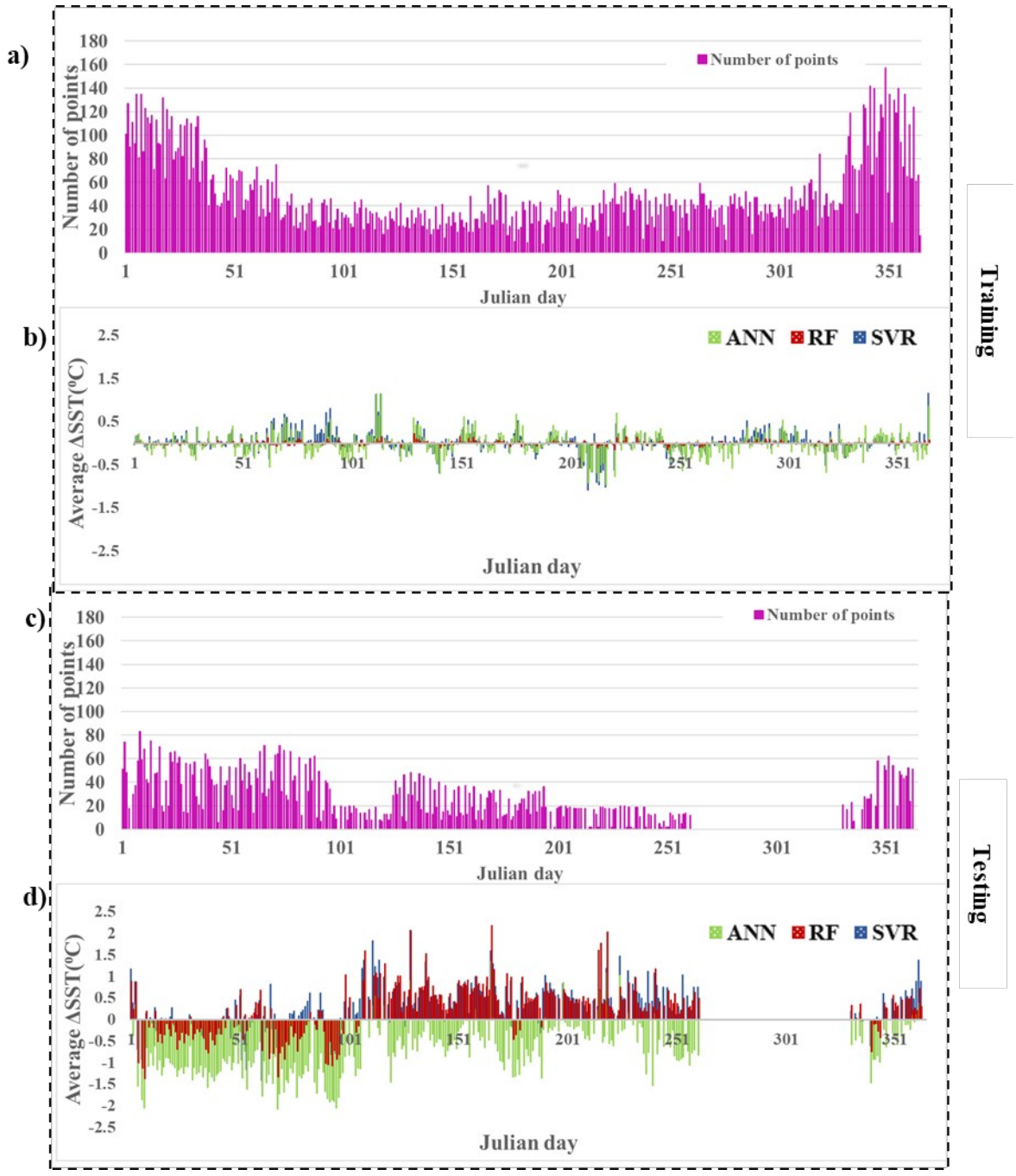

Figure 9: Number of reference points available in each Julian day and Average ΔSST ($SST_{ref} - \widehat{SST}$) in degree Celsius for the corresponding day during training (a-b) and testing(c-d) periods respectively for BOB.

Unlike AS, in BOB the training data for December, January and February are more abundant compared to the other months (Figure 9a). Even though there was large number of training data samples in the training period, all the developed algorithms underestimate during the first two months compared to other days in the testing period, which could be due to the temperature inversion happening in the winter as reported by Balachandran et al., 2008.

4.4 Inter-comparison of NOAA SST and the best performing ML SST

The results of inter-comparision between NOAA SST and the best performing ML algorithm (i.e. Scenario-1 SVR-SST) wrt in-situ data for the independent testing period (i.e. 2014-2015) in both the study regions are given in Table 2. Compared to the performance of SVR algorithm, the obtained results for NOAA SST shows higher correlation and lower error (i.e. RMSE and MAE) in both AS and BoB regions. It shall be noted that though the performance of SVR SST is lower to NOAA SST, the difference is not high (Table 2) especially in BoB. Moreover, the magnitude of the coefficient of determination and the error values for SVR SST presented in this study is better than that of the operational SST products viz. OSTIA, L3 and L4 MODIS SST evaluated by Thakur et al., 2018. Interestingly, the performance of NOAA SST is also relatively weak in BoB compared to AS region. It was observed that the RMSE values of SVR algorithm is almost close to the NOAA SST in BoB. It should be noted that the SVR SST derived in this study is of 1 km resolution, which is much finer than the NOAA SST which has 25 km resolution. The study conducted by Senatore et al, 2020 has proven that high resolution SST fields has significant impact on the simulation of the atmospheric boundary layer processes which in turn affect the forecast of hydrological responses to heavy precipitation. Therefore, even though NOAA SST is slightly performing better, SVR SST will be useful for studies similar to Senatore et al.,2020 which require high resolution SST.

Table:2 Performance of NOAA SST and SVR SST with respect to in situ data for AS and BoB for the period 2014-2015.

Statistics	Study Regions			
	AS		BoB	
	SVR	NOAA SST	SVR	NOAA SST
R^2_{adj}	0.82	0.90	0.78	0.83
RMSE (ºC)	0.71	0.62	0.88	0.88
MAE(ºC)	0.51	0.38	0.66	0.56

4.5 Illustrative examples of ML SST images

SST images obtained from the developed ML algorithms (for Scenario-1 case) were visually compared with the MODIS L2 SST and the NOAA SST products at their native resolutions. The in-situ datasets available on the corresponding day also overlayed on them. For illustrative purpose, the comparisons are shown for arbitrarily selected dates spanning different periods, viz. pre-monsoon, monsoon and post-monsoon in Figures 10–11, respectively.

4.5.1 Study Area I: AS

Illustrative examples of the SST images obtained from MODIS L2 SST, NOAA SST and ML SST algorithms for AS region during pre-monsoon, monsoon and post-monsoon period are shown in Figures 10 a-p. During the pre-monsoon period, MODIS L2 SST product is having huge gaps due to cloud cover (Figure 10a). For the same day, NOAA SST is able to capture the trends in SST variation but with coarser resolution (Figure 10b). ANN and RF algorithms are effective in capturing the overall trend, however, the SST images obtained from these two techniques are showing some discrepancies (Figures 10c & d) For example, the ANN-based estimates suffer from over smoothening and RF-based estimates are having horizontal as well as vertical patches of SST. The cloud-free SST image obtained using SVR algorithm (Figure 10e) shows values similar to MODIS L2 SST product but it covers whole region unlike MODIS SST. Visual comparison of SVR SST image and NOAA SST image indicates that

SVR SST product captures the minute variations in SSTs better than NOAA SST product due to its fine resolution. It is also observed that SVR algorithm performs much better than the other two tested ML techniques during the pre-monsoon season.

During the monsoon season, it can be seen that only very few pixels of SST is being retrieved from the MODIS L2 SST product due to intense cloud cover in the study area (Figure 10g). A typical example (Figures 10 g–k) illustrates that although the SST values from physical approach are very few, the machine learning-based approaches are able to retrieve the SST values without gaps. In this case too, the SVR algorithm gives a better representation of SST estimates compared to the other two tested algorithms. Likewise, during the post monsoon season too, the illustrative example given in Figures 10 (i-p) show that the performance of the tested SST products is similar to that in the pre-monsoon and monsoon seasons.

4.5.2 Study Area II: BoB

Illustrative example of SST images for BoB region during various seasons are given in Figures 11a-p. The results obtained are similar to AS region. During pre-monsoon (Figure 11a-f), monsoon (Figure 11g-k) and post-monsoon(Figure 11i-p) periods, ANN algorithm(Figure 11 c,i,n) fails to capture the overall treand and often deviated from the in situ data values. Even though RF algorithm (Figure d,j,o) is able to capture the overall trend, the images are looking patchy and distorted. SVR algorithm (Figure 11 f,k,p) is relatively better than the other two tested algorithms. It is to be noted that the SVR SST estimates are closely matching with the in situ dataset and the cloud free portions of MODIS L2 SST. Likewise, the NOAA SST values are also in good agreement with respect to the in situ data, however, they are having coarse resolution unlike SVR SST estimates.

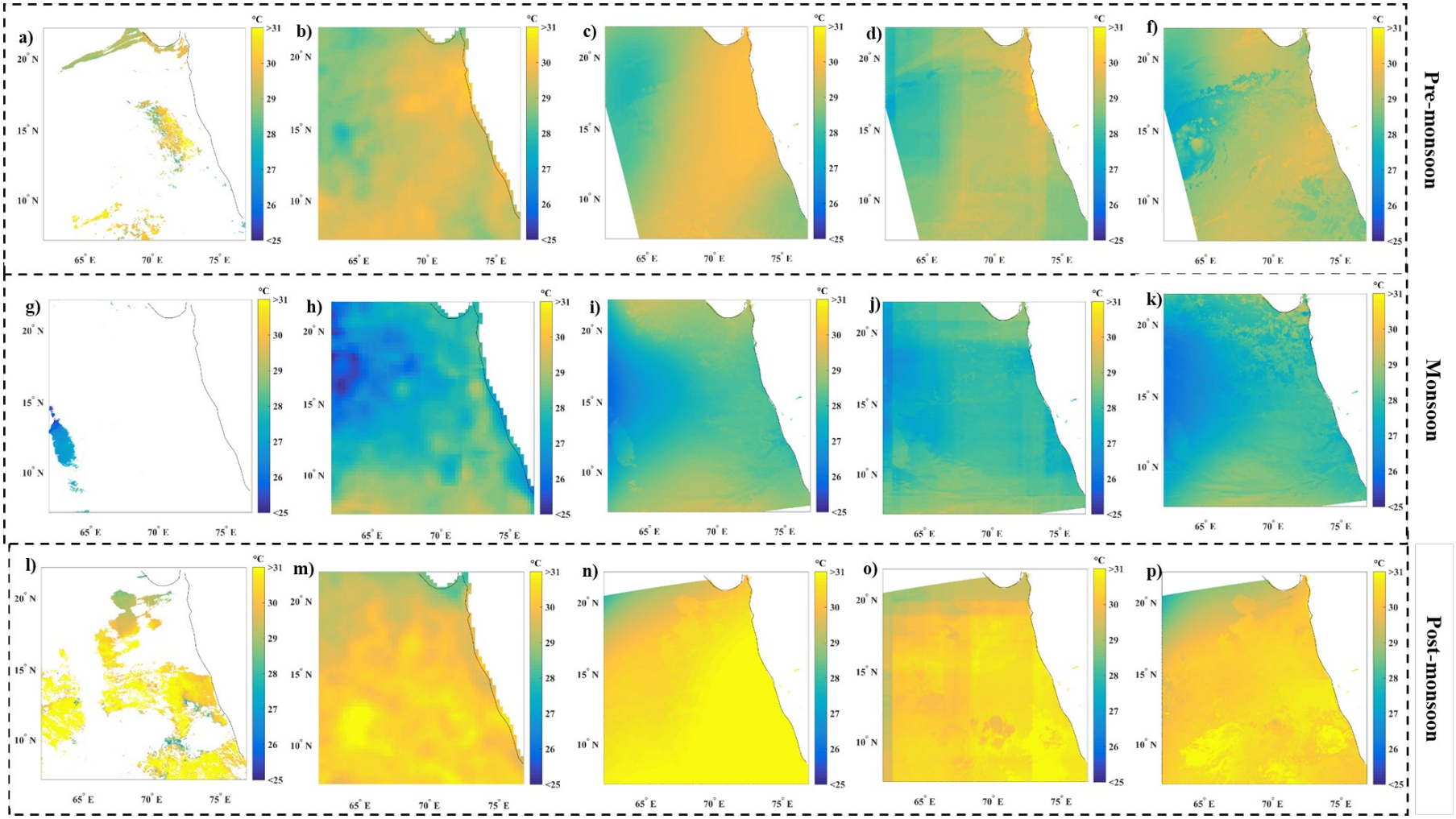

Figure 10: Illustrative example of ML based SSTs compared to the NOAA SST and MODIS L2 SST product for AS. (a)(g)(l) MODIS L2 SST, (b)(h)(m) NOAA SST and SST estimates from (c)(f)(n)ANN,(d)(J)(o) RF and (f)(k)(p)SVR machine learning algorithms during pre-monsoon,monsoon and post-monsoon. The in situ SST data available on the same day is overlayed on the product with the same color code.

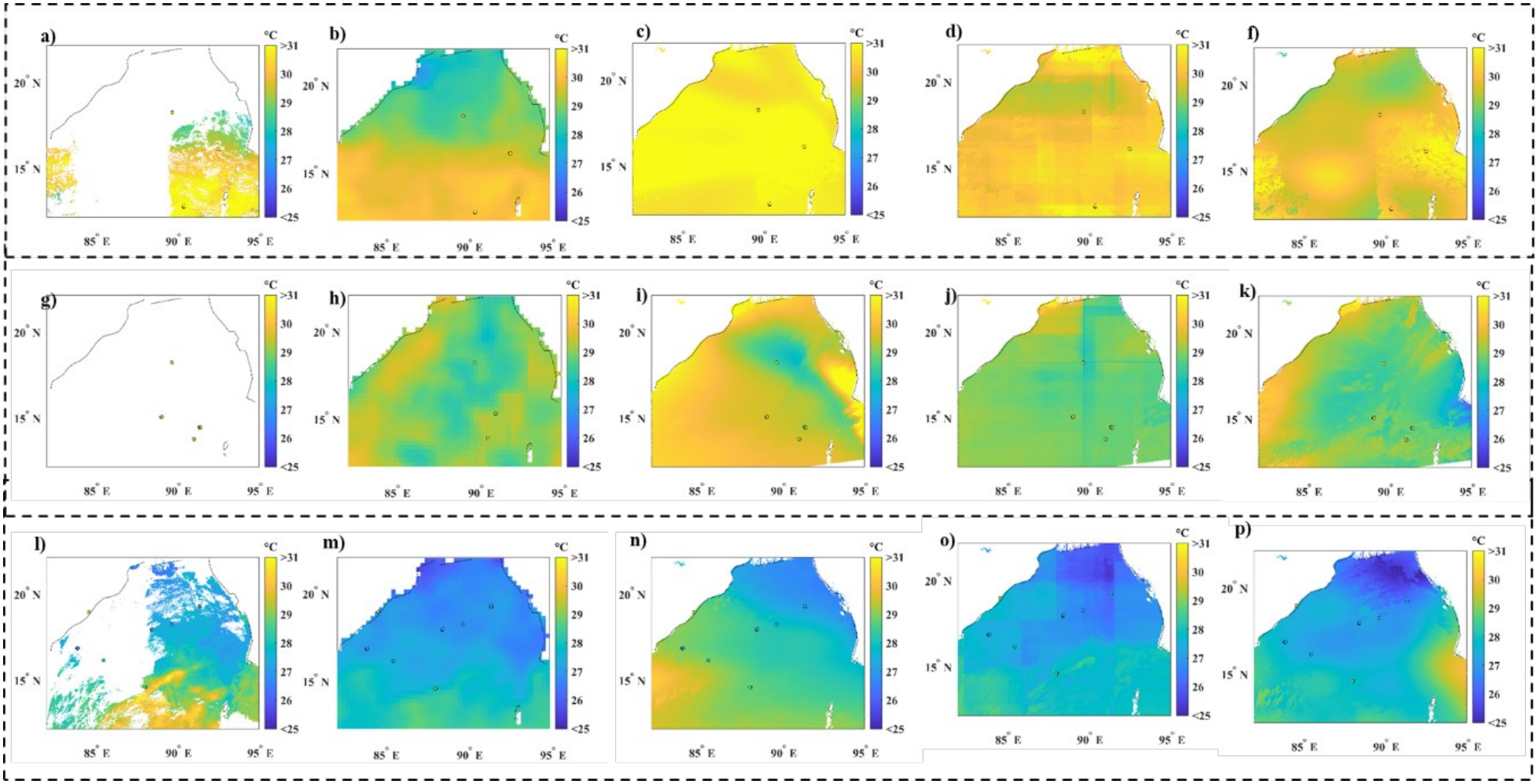

524

525 *Figure 11 : Illustrative example of ML-based SSTs compared to the NOAA SST and MODIS L2 SST product for BOB. (a)(g)(l) MODIS L2 SST, (b)(h)(m)*
526 *NOAA SST and SST estimates from (c)(f)(n)ANN,(d)(J)(o) RF and (f)(k)(p)SVR machine learning algorithms during pre-monsoon,monsoon and post-*
527 *monsoon. The in-situ SST data available on the same day is overlaid on the product with the same color code.*

Overall, the visual analysis of the ML SST estimates of different seasons indicates that SVR SST shows the best representation of SST compared to the other two ML algorithms. The primary reason behind the poor performance of RF and ANN techniques is their inability to capture minute differences in the latitude-longitude values. It is also observed that SVR SST and the operational NOAA SST and the cloud free regions of MODIS L2 SST products are having similar trends in SST variation for all three illustrative cases discussed here for both study areas.

Summary and Conclusions

This study is a first of its kind, to explore the potential of machine learning techniques to estimate cloud-free, high-resolution, accurate daily SST from a single IR sensor. In order to achieve this goal, three machine learning techniques viz. ANN, SVR and RF were explored for estimating SST from MODIS Aqua sensor dataset. The developed ML based algorithms were trained and tested for two different scenarios in two different study regions viz. Arabian Sea (AS) and Bay of Bengal (BOB). In Scenario-1, cloudy and non-cloudy pixels were trained and tested together, whereas in Scenario-2, the cloudy pixels and non-cloudy pixels were trained and tested separately. The obtained results when analysed with respect to in-situ data indicate Scenario-1 as the best scenario for all three ML algorithms and hence, this scenario results were further analysed in various aspects.

A spatio-temporal analysis of the difference between the ML-based SSTs and in-situ data (ΔSST) shows that SVR-based algorithm is more efficient compared to the other two ML algorithms. Futher, the best performing ML-based SST i.e. SVR SST was inter-compared with the operationl NOAA SST product of 25 km resolution. Compared to SVR SST, NOAA SST shows higher correlation and least error values with respect to in-situ data. However, SVR SST values are not significantly different from NOAA SST estimates for the same

552 period. At the same time, it is observed that the SVR algorithm is able to effectively capture
553 minute variations in SSTs better than NOAA SST as well as the other two ML algorithms.
554 Therefore, it can be concluded that the SVR is an effective technique for retrieving high-
555 resolution SST estimates even when the majority of the image is covered by cloud. Since all
556 the variables used in this approach are readily retrievable from satellite images immediately
557 after the satellite overpass, it can be used for near real-time applications; for example, as an
558 input to numerical models of various applications related to the ocean and weather
559 forecasting. This new algorithm based on SVR would be helpful to the on-going research
560 efforts by international research groups like GHRSST towards estimation of SST products at
561 finer resolution.

562 ## Acknowledegment

563 The authors would like to acknowledge the anonymous reviewers for their constructive
564 critisisims which helped us to improve our manuscript. The authours also thank CERSAT,
565 Ifermer for providing the in situ reference data. Additoanlly, authors would like to
566 acknowledge to NASA Goddard Space Flight Center, Ocean Ecology Laboratory, Ocean
567 Biology Processing Group for distrubuting the MODIS L0 dataset. The authors also would
568 like to thank NOAA National Centers for Environmental Information(NCEI) and PODAAC
569 for the free distribution of GHRSST Level 4 AVHRR_OI Global Blended Sea Surface
570 Temperature Analysis (GDS version 2).

571 ## References

572 Alavi, Amir H., Amir H. Gandomi, and David J. Lary. 2016. “Progress of Machine Learning
573 in Geosciences: Preface.” *Geoscience Frontiers* 7 (1): 1–2. doi:10.1016/j.gsf.2015.10.006.

574 Autret, E. and Piolle, J.F., 2011. Product User Manual for ODYSSEA Level 3 and 4 global

575 and regional products. MYO-PUM-SST-TAC-ODYSSEA, Ifremer/CERSAT.[Available
576 online at: http://projets. ifremer. fr/cersat/Data/Discovery/By-parameter/Sea-surface-
577 temperature/ODYSSEA-Global-SST-Analysis].

578 Baith, K., Lindsay, R., Fu, G. and McClain, C.R., 2001. Data analysis system developed for
579 ocean color satellite sensors. *Eos, Transactions American Geophysical Union*, *82*(18),
580 pp.202-202.

581 Balachandran, K.K., Laluraj, C.M., Jyothibabu, R., Madhu, N.V., Muraleedharan, K.R.,
582 Vijay, J.G., Maheswaran, P.A., Ashraff, T.M., Nair, K.K.C. and Achuthankutty, C.T., 2008.
583 Hydrography and biogeochemistry of the north western Bay of Bengal and the north eastern
584 Arabian Sea during winter monsoon. Journal of Marine Systems, 73(1-2), pp.76-86.

585 Barton, Ian J. 2001. "Interpretation of Satellite-Derived Sea Surface Temperatures."
586 *Advances in Space Research* 28 (1): 165–70. doi:10.1016/S0273-1177(01)00337-4.

587 Belgiu, Mariana, and Lucian Dra. 2016. "Random Forest in Remote Sensing : A Review of
588 Applications and Future Directions ", *ISPRS Journal of Photogrammetry and Remote Sensing*
589 114: 24–31. doi:10.1016/j.isprsjprs.2016.01.011.

590 Brasnett, B., 2008." The impact of satellite retrievals in a global sea−surface−temperature
591 analysis". *Quarterly Journal of the Royal Meteorological Society,* 134(636), pp.1745-1760.

592 Breiman, Leo. 2001. "Random Forests." *Machine Learning* 45 (1): 5–32.
593 doi:10.1023/A:1010933404324.

594 Brown, Otis B, and Peter J Minnett. 1999. "MODIS Infrared Sea Surface Temperature
595 Algorithm (ATBD 25, v2)." NASA Ocean Color [Available online at:
596 http://oceancolor.gsfc.nasa.gov/DOCS/atbd_mod25.pdf]

597 Buongiorno Nardelli, B., C. Tronconi, A. Pisano, and R. Santoleri. 2013. "High and Ultra-

598 High Resolution Processing of Satellite Sea Surface Temperature Data over Southern
599 European Seas in the Framework of MyOcean Project." *Remote Sensing of Environment* 129
600 (February): 1–16. doi:10.1016/j.rse.2012.10.012.

601 CERSAT.2018, Sea Surface Temperature In Situ Data [online].available at
602 http://cersat.ifremer.fr/data/tools-and-services/match-up-databases/item/298-sea-surface-
603 temperature-in-situ-data, accessed on 29/07/2018

604 Chao, Yi, Zhijin Li, John D. Farrara, and Peter Hung. 2009. "Blending Sea Surface
605 Temperatures from Multiple Satellites and in Situ Observations for Coastal Oceans." *Journal*
606 *of Atmospheric and Oceanic Technology* 26 (7): 1415–26. doi:10.1175/2009JTECHO592.1.

607 Chavula, Geoffrey, Patrick Brezonik, Prasad Thenkabail, Thomas Johnson, and Marvin
608 Bauer. 2009. "Estimating the Surface Temperature of Lake Malawi Using AVHRR and
609 MODIS Satellite Imagery." *Physics and Chemistry of the Earth* 34 (13–16). 749–54.
610 doi:10.1016/j.pce.2009.08.001.

611 Chin, Toshio Michael, Jorge Vazquez-Cuervo, and Edward M. Armstrong. 2017. "A Multi-
612 Scale High-Resolution Analysis of Global Sea Surface Temperature." *Remote Sensing of*
613 *Environment* 200 (July). 154–69. doi:10.1016/j.rse.2017.07.029.

614 Cracknell, Matthew J., and Anya M. Reading. 2014. "Geological Mapping Using Remote
615 Sensing Data: A Comparison of Five Machine Learning Algorithms, Their Response to
616 Variations in the Spatial Distribution of Training Data and the Use of Explicit Spatial
617 Information." *Computers and Geosciences* 63. 22–33. doi:10.1016/j.cageo.2013.10.008.

618 Dash, Prasanjit, Alexander Ignatov, Matthew Martin, Craig Donlon, Bruce Brasnett, Richard
619 W. Reynolds, Viva Banzon, et al. 2012. "Group for High Resolution Sea Surface
620 Temperature (GHRSST) Analysis Fields Inter-Comparisons-Part 2: Near Real Time Web-
621 Based Level 4 SST Quality Monitor (L4-SQUAM)." *Deep-Sea Research Part II: Topical*

Studies in Oceanography 77. 31–43. doi:10.1016/j.dsr2.2012.04.002.

David John Lary. 2010. "Artificial Intelligence in Geoscience and Remote Sensing." *Geoscience and Remote Sensing, New Achievements*, 1–24. doi:10.5772/51895.

Delgado, Ana L., Cédric Jamet, Hubert Loisel, Vincent Vantrepotte, Gerardo M.E. Perillo, and M. Cintia Piccolo. 2014. "Evaluation of the MODIS-Aqua Sea-Surface Temperature Product in the Inner and Mid-Shelves of Southwest Buenos Aires Province, Argentina." *International Journal of Remote Sensing* 35 (1). 306–20. doi:10.1080/01431161.2013.870680.

Donlon, Craig J., Matthew Martin, John Stark, Jonah Roberts-Jones, Emma Fiedler, and Werenfrid Wimmer. 2012. "The Operational Sea Surface Temperature and Sea Ice Analysis (OSTIA) System." *Remote Sensing of Environment* 116. 140–58. doi:10.1016/j.rse.2010.10.017.

Fablet, Ronan, Phi Viet, Redouane Lguensat, Pierre-Henri Horrein, and Bertrand Chapron. 2018. "Spatio-Temporal Interpolation of Cloudy SST Fields Using Conditional Analog Data Assimilation." *Remote Sensing* 10 (2): 310. doi:10.3390/rs10020310.

Joseph, K Ajith, T Thejna, and A N Balchand. 2007. "Studies on the Seasonal Variability of Chlorophyll-a Concentration and SST in the Eastern Arabian Sea Using Satellite Imageries" Journal Of Marine And Atmospheric Research (2): 41–50.

LaCasse, Katherine M., Michael E. Splitt, Steven M. Lazarus, and William M. Lapenta. 2008. "The Impact of High-Resolution Sea Surface Temperatures on the Simulated Nocturnal Florida Marine Boundary Layer." *Monthly Weather Review* 136 (4): 1349–72. doi:10.1175/2007mwr2167.1.

Lary, David J., Amir H. Alavi, Amir H. Gandomi, and Annette L. Walker. 2016. "Machine

645 Learning in Geosciences and Remote Sensing." *Geoscience Frontiers* 7 (1). 3–10.
646 doi:10.1016/j.gsf.2015.07.003.

647 Liu, Meiling, Xiangnan Liu, Jin Li, Chao Ding, and Jiale Jiang. 2014. "Evaluating Total
648 Inorganic Nitrogen in Coastal Waters through Fusion of Multi-Temporal RADARSAT-2 and
649 Optical Imagery Using Random Forest Algorithm." *International Journal of Applied Earth*
650 *Observation and Geoinformation* 33 (1). 192–202. doi:10.1016/j.jag.2014.05.009.

651 Liu, Meiling, Xiangnan Liu, Da Liu, Chao Ding, and Jiale Jiang. 2015. "Multivariable
652 Integration Method for Estimating Sea Surface Salinity in Coastal Waters from in Situ Data
653 and Remotely Sensed Data Using Random Forest Algorithm." *Computers & Geosciences* 75.
654 44–56. doi:10.1016/j.cageo.2014.10.016.

655 Maturi, Eileen, Andy Harris, Chris Merchant, Jon Mittaz, Bob Potash, Wen Meng, and John
656 Sapper. 2008. "NOAA's Sea Surface Temperature Products from Operational Geostationary
657 Satellites." *Bulletin of the American Meteorological Society* 89 (12): 1877–88.
658 doi:10.1175/2008BAMS2528.1.

659 Miles, Travis N., and Ruoying He. 2010. "Temporal and Spatial Variability of Chl-a and SST
660 on the South Atlantic Bight: Revisiting with Cloud-Free Reconstructions of MODIS Satellite
661 Imagery." *Continental Shelf Research* 30 (18). 1951–62. doi:10.1016/j.csr.2010.08.016.

662 Moser, Gabriele and Sebastiano B Serpico. 2009. "Automatic Parameter Optimization for
663 Support Vector Regression for Land and Sea Surface Temperature Estimation From Remote
664 Sensing Data", *IEEE Transactions on Geoscience and Remote Sensing* , 47 (3): 909–21.

665 Mountrakis, Giorgos, Jungho Im, and Caesar Ogole. 2011. "Support Vector Machines in
666 Remote Sensing: A Review." *ISPRS Journal of Photogrammetry and Remote Sensing* 66 (3).
667 Elsevier B.V.: 247–59. doi:10.1016/j.isprsjprs.2010.11.001.

NCEI. 2016. GHRSST Level 4 AVHRR_OI Global Blended Sea Surface Temperature Analysis (GDS version 2) from NCEI. Ver. 2.0. PO.DAAC, CA, USA. Dataset last accessed 29-08-2018 at http://dx.doi.org/10.5067/GHAAO-4BC02

NASA. 2019, Cloud Climatology, Global Distribution and Character of Clouds.[online] Avaliable at https://www.giss.nasa.gov/research/briefs/rossow_01/distrib.html, [Accessed 05 May,2019].

NASA Goddard Space Flight Center, Ocean Biology Processing Group. 2014. Moderate-resolution Imaging Spectroradiometer (MODIS) Aqua Level 0 Data; NASA OB.DAAC, Greenbelt, MD, USA. Available at : https://oceandata.sci.gsfc.nasa.gov/MODIS-Aqua/L0/, Accessed on 29/01/2018. Maintained by NASA Ocean Biology Distibuted Active Archive Center (OB.DAAC), Goddard Space Flight Center, Greenbelt MD.

Newman, S. M., J. a. Smith, M. D. Glew, S. M. Rogers, and J. P. Taylor. 2005. "Temperature and Salinity Dependence of Sea Surface Emissivity in the Thermal Infrared." *Quarterly Journal of the Royal Meteorological Society* 131: 2539–57. doi:10.1256/qj.04.150.

Picart, Stéphane Saux, Pierre Tandeo, Emmanuelle Autret, and Blandine Gausset. 2018. "Exploring Machine Learning to Correct Satellite-Derived Sea Surface Temperatures." *Remote Sensing* 10 (2): 1–11. doi:10.3390/rs10020224.

Reynolds, Richard W., and Dudley B. Chelton. 2010. "Comparisons of Daily Sea Surface Temperature Analyses for 2007-08." *Journal of Climate* 23 (13): 3545–62. doi:10.1175/2010JCLI3294.1.

Reynolds, Richard W., Thomas M. Smith, Chunying Liu, Dudley B. Chelton, Kenneth S. Casey, and Michael G. Schlax. 2007. "Daily High-Resolution-Blended Analyses for Sea Surface Temperature." *Journal of Climate* 20 (22): 5473–96. doi:10.1175/2007JCLI1824.1.

691 RSS (2019), Research-Quality Geophysical Products From Satellite Microwave Sensors.
692 [online] Avaliable at http://remss.com/, [Accessed 05May.2019].

693 Santos, A. Miguel P. 2000. “Fisheries Oceanography Using Satellite and Airborne Remote
694 Sensing Methods: A Review.” *Fisheries Research* 49 (1): 1–20. doi:10.1016/S0165-
695 7836(00)00201-0.

696 Senatore, A., Furnari, L. and Mendicino, G., 2020. Impact of high-resolution sea surface
697 temperature representation on the forecast of small Mediterranean catchments' hydrological
698 responses to heavy precipitation. Hydrology and Earth System Sciences, 24(1), pp.269-291.

699 Shenoi, S.S.C., Shankar, D. and Shetye, S.R., 2002. Differences in heat budgets of the near−
700 surface Arabian Sea and Bay of Bengal: Implications for the summer monsoon. Journal of
701 Geophysical Research: Oceans, 107(C6), pp.5-1.

702 Sirjacobs, Damien, Aida Alvera-Azcárate, Alexander Barth, Geneviève Lacroix, YoungJe
703 Park, Bouchra Nechad, Kevin Ruddick, and Jean-Marie Beckers. 2011. “Cloud Filling of
704 Ocean Colour and Sea Surface Temperature Remote Sensing Products over the Southern
705 North Sea by the Data Interpolating Empirical Orthogonal Functions Methodology.” *Journal*
706 *of Sea Research* 65 (1): 114–30. doi:10.1016/j.seares.2010.08.002.

707 Stark, John D., C. Donlon, A. O’Carroll, and G. Corlett. 2008. “Determination of AATSR
708 Biases Using the OSTIA SST Analysis System and a Matchup Database.” *Journal of*
709 *Atmospheric and Oceanic Technology* 25 (7): 1208–17. doi:10.1175/2008JTECHO560.1.

710 Thadathil, P. and Gosh, A.K., 1992. Surface layer temperature inversion in the Arabian Sea
711 during winter. Journal of Oceanography, 48(3), pp.293-304.

712 Thakur, K.K., Vanderstichel, R., Barrell, J., Stryhn, H., Patanasatienkul, T. and Revie, C.W.,
713 2018. Comparison of remotely-sensed sea surface temperature and salinity products with in

situ measurements from British Columbia, Canada. Frontiers in Marine Science, 5, p.121.

Tomažić, I., M. Kuzmić, G. Notarstefano, E. Mauri, and P. M. Poulain. 2011. "A Comparative Assessment of Satellite-Derived Adriatic Sea Surface Temperature." *International Journal of Remote Sensing* 32 (17): 4871–92. doi:10.1080/01431161.2010.492249.

Tomazic, I, M Kuzmic, G Notarstefano, E Mauri, and P M Poulain. 2011. "A Comparative Assessment of Satellite-Derived Adriatic Sea Surface Temperature." *International Journal of Remote Sensing* 32 (17): 4871–92. doi:Doi 10.1080/01431161.2010.492249.

Vapnik, V., 1979. Estimation of Dependences Based on Empirical Data. Nauka, Moscow, pp. 5165–5184, 27 (in Russian) (English translation: Springer Verlag, New York, 1982)

Wang, Jiao, and Zhiqiang Deng. 2017. "Development of MODIS Data-Based Algorithm for Retrieving Sea Surface Temperature in Coastal Waters." *Environmental Monitoring and Assessment* 189 (6). Environmental Monitoring and Assessment. doi:10.1007/s10661-017-6010-7.

Williams, G., M. Sapoznik, M. Ocampo-Reinaldo, M. Solis, M. Narvarte, R. González, J. L. Esteves, and D. Gagliardini. 2010. "Comparison of AVHRR and SeaWiFS Imagery with Fishing Activity and in Situ Data in San Matías Gulf, Argentina." *International Journal of Remote Sensing* 31 (17): 4531–42. doi:10.1080/01431161.2010.485218.

Witten, Ian H, Eibe Frank, Mark A Hall, and Christopher J Pal. 2016. *Data Mining: Practical Machine Learning Tools and Techniques*. Morgan Kaufmann.

Zhao, Yao, and Ruoying He. 2012. "Cloud-Free Sea Surface Temperature and Colour Reconstruction for the Gulf of Mexico: 2003–2009." *Remote Sensing Letters* 3 (8): 697–706. doi:10.1080/01431161.2012.666638.

737